

Multiband Photoresponding Field-Effect Transistor Memory Using Conjugated Block Copolymers with Pendent Isoindigo Coils as a Polymer Electret

Chen-Fu Lin, Yan-Cheng Lin,* Wei-Chen Yang, Li-Che Hsu, Ender Ercan, Chih-Chien Hung, Yang-Yen Yu,* and Wen-Chang Chen*

In this study, the authors report a series of conjugated block copolymers, PF-*b*-Piso comprising poly[2,7-(9,9-dihexylfluorene)] (PF), and poly(pendent isoindigo) (Piso) for polymer electret in the photonic field-effect transistor (FET) memory device. The optical properties, surface morphology, and molecular organization of these BCPs are investigated systematically. Accordingly, Piso with absorption in the Ultraviolet C range (UVC, 200–280 nm) possibly rendered the device with a multiband photoresponse, and a good memory performance is achieved by optimizing the polymer composition. Therefore, the memory device comprising PF-*b*-Piso could perform a high current contrast of 10^6 to 40^5 nm light and 10^5 to 254 nm light over 10^4 s. In addition, a current contrast of 10^4 and 10^2 is achieved in response to 650 and 530 nm light, and this phenomenon can be attributed to the charge transfer between channel and memory layers. The experimental results indicate that the block copolymer design not only conduces to forming a self-assembled microphase separation to stabilize the trapped charge in the polymer electret, but also triggers multiband photoresponding of the photonic FET memory.

non-destructive read-out, photo-assisted programming, multibit data storage, and high compatibility with integrated circuits composed of FETs.^[1–4] FET memory devices with polymer electrets outperform their inorganic counterparts in their affordability, being light-weight, mechanical flexibility, diversified structural design, etc.^[5–8] Especially, photonic FET memory, in addition to the aforementioned advantages, currently presents a high current contrast (10^5), fast programming time (<3 s), and prolonged retention time ($>10^4$ s), etc.^[9–12]

Many design strategies have been proposed concerning the plethora of the charge trapping materials including an organic–inorganic hybrid floating gate,^[13,14] a conjugated/insulating polymer blends based floating gate,^[15,16] rod-coil molecules with highly order layer structure,^[17,18] donor–acceptor copolymers,^[19–21] conjugated block copolymers (BCPs),^[22] or

charge-transfer supramolecules^[23] as polymer electrets. Among them, polyfluorene (PF)-based BCPs are multifunctional with its favorable energy level adaption with channel materials like pentacene or dinaphthothienothiophene, and decent photoresponse along with their semiconducting properties.^[24–26] Especially, the current leakage from the electret to channel layer due to the extension in π -conjugation of the PF backbone can be efficiently assuaged by forming microphase separation with an insulating polymer segment.^[22,27–29] Therefore, PF-based BCPs with polystyrene (PS) coils (PF-*b*-PS) were evidenced as a high-performing polymer electret in photonic FET memory with a current contrast of 10^4 over 10^4 s.^[22]

Previously, our group proposed a series of PF-based BCPs with poly(pendent isoindigo) (Piso) coils (PF-*b*-Piso) as the electret for stretchable memristor.^[30] The device was fabricated by integrating PF-*b*-Piso on a soft PDMS substrate with a high ON/OFF ratio of 10^5 under 0–50% applied tensile strain. The studied BCPs combined the conjugated rods for superior electronic properties and pendent isoindigo coils for enhanced material ductility. Yet, it is of great interest to understand the efficacy of insulating coil with the photoresponding moiety in the photonic FET memory. In addition, there is no study about the BCP electret with electron accepting moiety in the insulating coil, and it is reported that Piso is a good electron acceptor.^[30] With the electron acceptor inside the BCP electret

1. Introduction

In the past decade, there has been growing research interest in field-effect transistor-type (FET) memory owing to its

C.-F. Lin, Y.-Y. Yu

Department of Materials Engineering

Ming Chi University of Technology

New Taipei City 24301, Taiwan

E-mail: yyyu@mail.mcut.edu.tw

Y.-C. Lin, W.-C. Yang, E. Ercan, W.-C. Chen

Department of Chemical Engineering

National Taiwan University

Taipei 10617, Taiwan

E-mail: ycl2020@ntu.edu.tw; chenwc@ntu.edu.tw

Y.-C. Lin, E. Ercan, C.-C. Hung, W.-C. Chen

Advanced Research Center of Green Materials Science and Technology

National Taiwan University


Taipei 10617, Taiwan

L.-C. Hsu

Institute of Polymer Science and Engineering

National Taiwan University

Taipei 10617, Taiwan

 The ORCID identification number(s) for the author(s) of this article can be found under <https://doi.org/10.1002/aelm.202100655>.

DOI: 10.1002/aelm.202100655

in the photonic FET memory, the photogenerated charge could be stabilized and render a better photowriting performance. Based on this rationale, we herein are intended to introduce PF-*b*-Piso into photonic FET memory as a polymer electret by utilizing the optical absorption of Piso in Ultraviolet C (UVC, 200–280 nm), and PF in Ultraviolet A (UVA, 320–400 nm) and blue light to endow multiband photoresponding.

In this work, a series of PF-*b*-Piso BCPs with various Piso content (i.e., PF-*b*-Piso₁₀, PF-*b*-Piso₂₀, PF-*b*-Piso₆₀, and PF-*b*-Piso₁₀₀) was studied with their optics-photoresponse properties in the photonic FET memory. To gain insight into PF-*b*-Piso, optical properties with UV-vis absorption and photoluminescence (PL) emission, morphological properties with atomic force microscopy (AFM), grazing-incidence small-angle X-ray scattering (GISAXS), and grazing-incidence wide-angle X-ray scattering (GIWAXS) were evaluated, and their optics-photoresponse properties in the photonic FET memory were systematically corroborated. We found that Piso coils are conducive to forming a self-assembled microphase separation, stabilizing trapped charge in the polymer electret, associated with a triggering multiband photoresponse. This research provides an effective way to design polymer electret containing the optimal ratio of conjugated and insulating polymers exhibiting decent photonic performance with a high current contrast of 10⁶ to 405 nm light and 10⁵ to 254 nm light over 10⁴ s.

2. Results and Discussion

2.1. Materials Characterization

PF-*b*-Piso BCPs were prepared by using the click reaction of copper-catalyzed azide-alkyne cycloadditions (CuAAC) with

ethyne-terminated PF block ($M_{n,NMR} = 4900$) and azide-terminated Piso block with $M_{n,NMR} = 4900, 9900, 29\,800,$ and $53\,700$ for PF-*b*-Piso₁₀, PF-*b*-Piso₂₀, PF-*b*-Piso₆₀, and PF-*b*-Piso₁₀₀, respectively. The BCPs studied exhibited glass transition temperature (T_g) of 74, 78, 82, and 84 °C for PF-*b*-Piso₁₀, PF-*b*-Piso₂₀, PF-*b*-Piso₆₀, and PF-*b*-Piso₁₀₀, respectively, which were determined from DSC thermal histograms, as seen in our previous work.^[30] Therefore, the BCP thin films were annealed at 100 °C to form a favorable morphology of microphase separation.

Figure 1a depicts the chemical structures of the channel material, polymer electret, and the device configuration of the photonic FET memory in this study. In order to understand the optics-photoresponse properties of the BCP electrets in the photonic FET memory, UV-vis absorption analysis were conducted, as seen in Figure 1b. The studied BCPs exhibited two distinct absorption bands with 350–410 nm for PF and 250–300 nm for Piso. Piso with absorption in the UVC range possibly rendering the device with additional functionality to achieve multiband light absorption and memory behavior. Besides, pentacene was selected as the channel material due to its non-overlapping absorption with the BCP electret and high carrier mobility. PL emission study was conducted to understand the charge-generation, -separation, and -transfer in the BCP films, and the spectra of these BCPs are presented in Figure S1, Supporting Information. As can be seen, the BCP films possess PL emission at 400–500 nm with an excitation wavelength of 365 nm, and this emission was contributed from the PF block. In contrast, the BCP films showed no PL emission with an excitation wavelength of 254 nm, indicating the photoinduced excitons were easily quenched in the Piso block. Therefore, it is postulated that the photoinduced excitons in the Piso block were easily separated and transferred

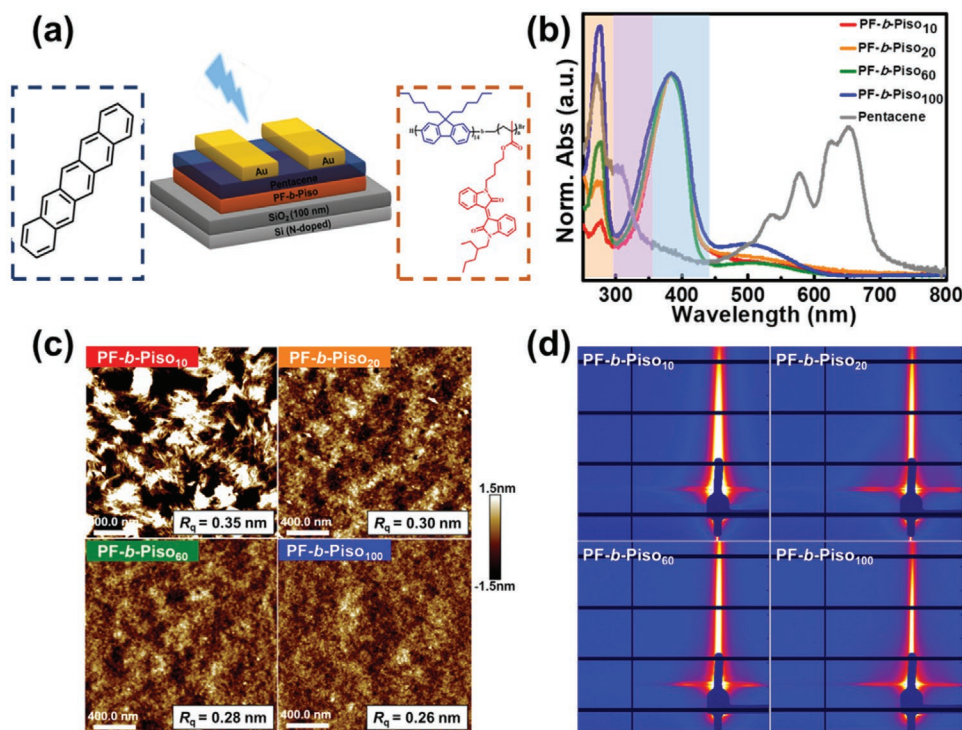


Figure 1. a) Device architecture and chemical structure of the materials in the channel and memory layers. b) UV-vis absorption spectra of PF-*b*-Piso and pentacene. c) AFM topographies and d) 2D GISAXS patterns of the thermally annealed BCP films.

into charges. Next, the frontier molecular orbital energy levels of the homogeneous polymers (PF and Piso) and BCPs are presented in Table S1, Supporting Information. The highest occupied molecular orbital (HOMO) levels and the lowest unoccupied molecular orbital (LUMO) levels are (−5.48, −2.69) V, (−5.55, −2.71) V, (−5.74, −2.76) V, (−5.84, −2.84) V, (−6.06, −3.00) V, and (−6.24, −2.96) V for PF, PF-*b*-Piso₁₀, PF-*b*-Piso₂₀, PF-*b*-Piso₆₀, PF-*b*-Piso₁₀₀, and Piso, respectively. It is understood that the difference in HOMO levels between PF and pentacene can prevent carrier back-trapping; while a lower-lying LUMO level of insulating segment (Piso) compared to PF is favorable for stabilizing trapped charges.^[22]

2.2. Morphological Characterization of the BCP Thin Films

In order to mitigate the current leakage from the PF backbone to the channel of pentacene, Piso with soft coil segment was introduced to form a microphase separated morphology with PF. To gain insight into the morphology-photoresponse properties in these BCP thin films, morphological characterization was next evaluated. Figure S2, Supporting Information, and Figure 1c present the AFM topographies of the as-cast and thermally annealed BCP films. As seen, the surface of these BCPs become more homogeneous after thermal annealing, and the surface roughness of the annealed PF-*b*-Piso₁₀, PF-*b*-Piso₂₀, PF-*b*-Piso₆₀, and PF-*b*-Piso₁₀₀ were 0.35, 0.30, 0.28, and 0.26 nm, respectively. As the Piso content increased, the surface became smoother, and this behavior may be attributed to the introduction of longer Piso coil segments to mitigate the self-aggregation of PF. These findings show that Piso content plays an important role in forming homogeneous nanoclusters and a highly crystalline pentacene channel. Compared to our previous work about the application of PF-*b*-Piso in the stretchable memristor, a low boiling point of chloroform was used to spin coat the PF-*b*-Piso film, and a nanofibrillar morphology was formed to promote the stretchability of the film.^[30] However, it was observed that the nanofibrils with a strong aggregation of PF would easily induce charge recombination and deteriorate the memory performance.^[22] Therefore, a high boiling point solvent of chlorobenzene was used to achieve nanocluster morphology in the PF-*b*-Piso films.

AFM morphology can only provide a general aspect of polymer chain arrangement, and thus the in-depth domain definition and molecular stacking pattern should be further corroborated by using GISAXS and GIWAXS analyses. Figure S3a, Supporting Information, and Figure 1d showed the 2D GISAXS patterns of the as-cast and thermally annealed BCP films, respectively. The 1D GISAXS profiles of the as-cast and thermally annealed films with q_y scan at $q_z = 0.027 \text{ \AA}^{-1}$ were derived and are presented in Figure S3b and S3c, Supporting Information, respectively. As seen, PF-*b*-Piso₁₀ did not exhibit an obvious self-assembled structure. Intriguingly, a self-assembled domain can be seen in PF-*b*-Piso₂₀ and PF-*b*-Piso₆₀ with a respective domain size of 21.6 and 26.9 nm. However, PF-*b*-Piso₁₀₀ presents a less propensity in forming self-assembly. This phenomenon might indicate that Piso coils can effectively disperse PF, while an excessive Piso coil would easily degrade the morphological order. Next, Figures S4a,b and S4c,d,

Supporting Information, presents the 2D GIWAXS patterns and 1D GIWAXS profiles of the as-cast and thermally annealed BCP films. As seen, there was no stacking signal in the as-cast BCP films. As the films were thermally annealed, PF-*b*-Piso₁₀ presents several obvious diffractions of (200), (220), and (420). In contrast, a weaker propensity in forming crystallographic patterns can be observed for BCPs with a higher Piso content. This result might indicate that PF are prone to aggregate and stack with fewer Piso coils. All the morphological characterization underlines the importance of Piso coils for the efficient dispersion of PF and the formation of homogeneous, microphase separated morphology. It is understood that the ratio between the conjugated and insulating segments in PF-*b*-Piso could pivotally affect the charge storage and photoresponse efficacy in the electret of photonic FET memory, and this issue will be discussed in the next paragraph.

2.3. Photonic FET Memory Device Characterization

After elucidating the morphology-optics properties of these BCP films, the structure-photoresponse relationship of BCP electrets were next studied. A bottom-gate top-contact (BG/TC) device configuration was adopted in the photonic FET memory, and BCPs were introduced as polymer electrets between the channel layer and the dielectric layer. Transfer characteristics of the photonic FET memory with the annealed BCP electrets were conducted and presented in Figure 2a,d for PF-*b*-Piso₁₀, PF-*b*-Piso₂₀, PF-*b*-Piso₆₀ and PF-*b*-Piso₁₀₀, respectively. In addition, transfer characteristics of the reference devices with pentacene only or PF as electret are displayed in Figure S6a,b, Supporting Information. Transfer characteristics were recorded by sweeping the gate voltage (V_g) from −20 to 40 V. The photowriting of the devices were conducted by illuminating blue light (405 nm), UVC (254 nm), and UVA light (365 nm) for 20 s, and the drain current was collected at $V_d = -40$ V. The electrical erasing was performed with V_g of −40 V for 1 s. The resultant device parameters derived from transfer curves are summarized in Table 1 and the device parameters of the reference devices are presented in Table S2, Supporting Information. The photonic FET memory devices with pentacene channel typically exhibited p-type transfer curves with a hole mobility (μ_h) of 0.011–0.025 cm² V^{−1} s^{−1}, which were comparable to the μ_h of the pentacene only device of 0.027 cm² V^{−1} s^{−1}. Among them, the device with PF-*b*-Piso₂₀ electret exhibited the highest μ_h of 0.025 cm² V^{−1} s^{−1}, due to the larger pentacene grain grown on the electret as seen in Figure S5, Supporting Information. In contrast, the reference device with PF as electret showed a much lower μ_h of 0.007 cm² V^{−1} s^{−1} due to the hole trapping capability of PF. Next, as the photowriting process was applied, a clear electron-trapping propensity was observed to render ON-state. As giving a negative gate bias, the memory devices were electrically erased into an OFF-state. The threshold voltage (V_{th}) in the 405 nm light written, 254 nm light written ON-state, and electrically erased OFF-state were (1, −4, −27), (7, 0, −26), (3, 0, −27), and (1, −3, −26) for PF-*b*-Piso₁₀, PF-*b*-Piso₂₀, PF-*b*-Piso₆₀, and PF-*b*-Piso₁₀₀, respectively. A large memory window (ΔV_{th}) of PF-*b*-Piso₂₀ and PF-*b*-Piso₆₀ can be observed with 405 and 254 nm photowriting compared to PF-*b*-Piso₁₀ and PF-*b*-Piso₁₀₀.

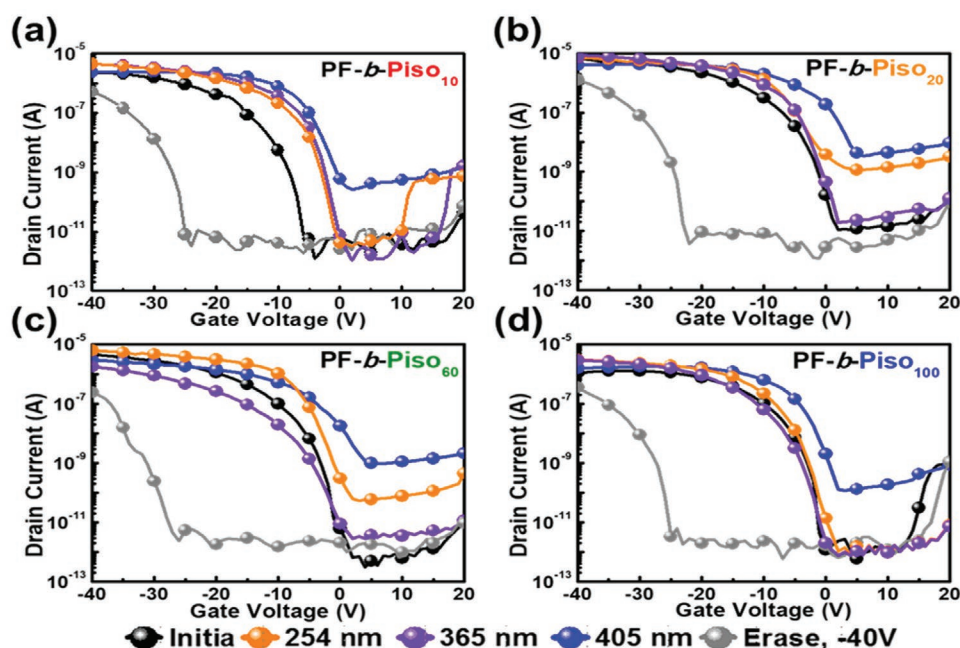


Figure 2. Transfer characteristics of photonic FET memory with a) PF-*b*-Piso₁₀, b) PF-*b*-Piso₂₀, c) PF-*b*-Piso₆₀, and d) PF-*b*-Piso₁₀₀ as electret. The drain current was measured at $V_d = -40$ V when applying photo-writing or electrical erasing (-40 V; 1 s).

This indicates that Piso coils can effectively disperse PF in the microphase separated morphology to perform a better charge storage. Therefore, PF-*b*-Piso₂₀ and PF-*b*-Piso₆₀ present higher memory ratio (I_{on}/I_{off}) of 10^5 and 10^4 , outperforming 10^2 for PF-*b*-Piso₁₀ and PF-*b*-Piso₁₀₀. Although the electrical erasing gave rise to a lower ON-state current and μ_h in the memory device, it could be fast recovered by the subsequent photowriting process. As seen in the transfer characteristics of the reference device with PF as electret (Figure S6a,b, Supporting Information), the memory device was repeatedly photowritten with various wavelengths of light and electrically erased with gate bias, and the photoinduced exciton could split into an electron/hole pair and electrons could repetitively recombine with the trapped hole in the BCP film. Next, the as-cast BCP films present a decreased

response in photowriting as seen in the transfer characteristics of the photonic FET memory devices with the as-cast electret (Figure S7a–d, Supporting Information). Still, PF-*b*-Piso₂₀ and PF-*b*-Piso₆₀ surpass other BCPs with a good I_{on}/I_{off} of 10^3 compared to 10^1 – 10^2 for PF-*b*-Piso₁₀ and PF-*b*-Piso₁₀₀. Notably, multi-band photoresponding was successfully fulfilled in these BCP electrets with PF active to blue to UVA band and Piso active to UVC band.

Transient characteristics of the devices with annealed BCP electrets were evaluated at $V_d = -60$ V and proceeded with photo writing for 20 s, as seen in Figure 3a,d for PF-*b*-Piso₁₀, PF-*b*-Piso₂₀, PF-*b*-Piso₆₀, and PF-*b*-Piso₁₀₀, respectively. It can be clearly seen that PF-*b*-Piso₂₀ presents the most stable and distinguishable photoresponse with I_{on}/I_{off} of 10^5 , 10^3 , and 10^4 to 405, 365, and 254 nm light, respectively. Different levels of ON-state current conferred by varied light illumination were beneficial for multibit data storage application and improving data discriminability of the photonic FET memory. Compared to the as-cast electret, PF-*b*-Piso₂₀ presents a better I_{on}/I_{off} of 10^4 , 10^1 , and 10^3 to 405, 365, and 254 nm light, respectively, compared to other BCPs electrets in the transient characteristics (Figure S8a–d, Supporting Information). The photosensitivity (P) and photoresponsivity (R) of these devices with BCP electrets were calculated and are summarized in Table S3, Supporting Information. As can be seen, PF-*b*-Piso₂₀ presented the highest P and R ($A W^{-1}$) of $(5.5 \times 10^5, 0.028)$ and $(3.6 \times 10^4, 0.059)$ with 405 and 254 nm light illumination. In contrast, PF-rich BCP of PF-*b*-Piso₁₀ presented a lower R of $3.6 \times 10^{-4} A W^{-1}$ to 405 nm light, and Piso-rich BCP of PF-*b*-Piso₁₀₀ presented a negligible R of $6.1 \times 10^{-5} A W^{-1}$ to 254 nm light. Notably, PF-*b*-Piso₂₀ presented a higher R to 254 nm light than 405 nm light. Combining with observation from PL spectra that Piso presented no emission at 254 nm light, it is postulated that the photoinduced

Table 1. Device parameters of the photonic FET memory devices with BCP-based electret.

	λ [nm]	PF- <i>b</i> -Piso ₁₀	PF- <i>b</i> -Piso ₂₀	PF- <i>b</i> -Piso ₆₀	PF- <i>b</i> -Piso ₁₀₀
μ_h [$cm^2 V^{-1} s^{-1}$]	–	0.021	0.025	0.011	0.018
$V_{th,erase}$ [V]	–	–27	–26	–27	–26
I_{on}/I_{off}	405 nm	10^2	10^5	10^4	10^2
	365 nm	10^1	10^3	10^3	10^1
	254 nm	10^1	10^4	10^3	10^1
$V_{th,write}$ [V]	405 nm	1	7	3	1
	365 nm	–5	–1	–3	–6
	254 nm	–4	0	0	–3
ΔV_{th} [V]	405 nm	28	33	30	27
	365 nm	22	25	24	20
	254 nm	23	26	27	23

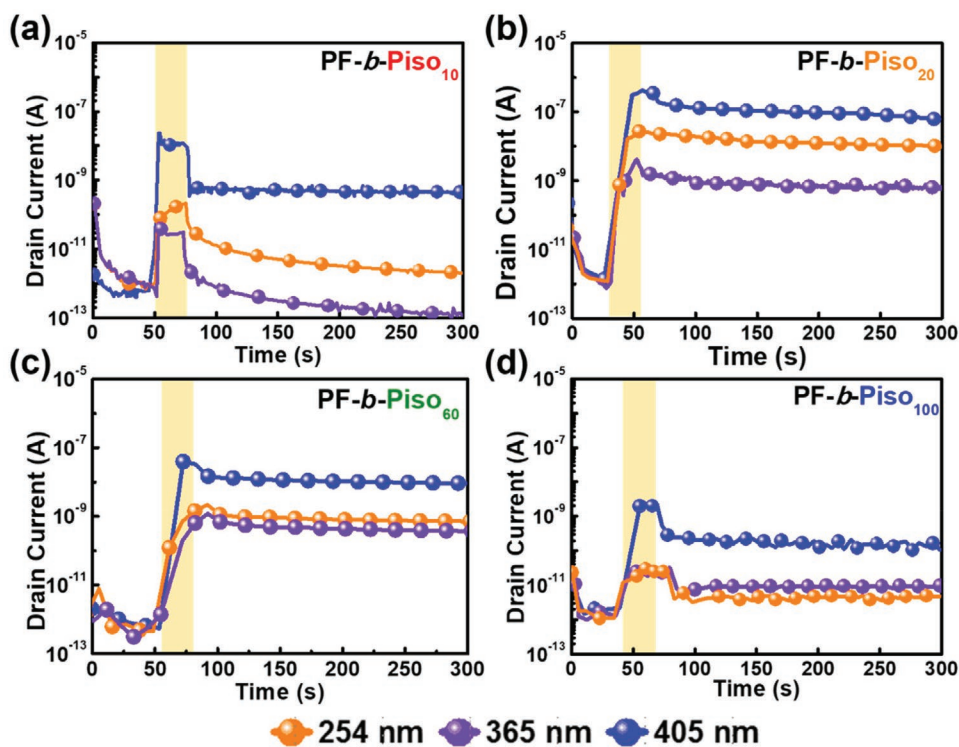


Figure 3. Transient characteristics of photonic FET memory with a) *PF-b-Piso*₁₀, b) *PF-b-Piso*₂₀, c) *PF-b-Piso*₆₀, and d) *PF-b-Piso*₁₀₀ as electrets. The photo-writing was conducted with varied light for 20 s, and the drain current was measured at $V_d = -60$ V and $V_g = 0$ V.

excitons in the Piso block were easily separated and transferred into charges, and therefore render a stronger photoresponse in the photonic FET memory. These results manifest *PF-b-Piso*₂₀ with an optimized Piso content is conducive to forming self-assembled microphase separation, stabilizing trapped charge in the polymer electret, associated with triggering multiband photoresponding. In contrast, the reference devices with pentacene only or PF as electret under pentacene showed no shift in transfer curves (Figure S6a,b, Supporting Information), a weak photoresponse and no memory behavior (Figure S6c,d, Supporting Information) with various wavelength of light illumination, and the current contrast was slightly higher with PF as an electret compared to the pentacene-only device. This phenomenon corroborated the necessity of the BCP design to efficiently charge transfer and the efficacy of Piso to mitigate the severe hole trapping from PF and promote electron stabilization.

To illustrate the memory stability and switching endurance, the devices were tested with long-term retention, as seen in Figure 4a for *PF-b-Piso*₂₀ and Figure S9a–c, Supporting Information, for *PF-b-Piso*₁₀, *PF-b-Piso*₆₀, and *PF-b-Piso*₁₀₀, respectively. Retention test were conducted at $V_d = -60$ V for 10 000 s with varied light illumination. As seen, *PF-b-Piso*₂₀ presents a better I_{on}/I_{off} of 10^6 , 10^4 , and 10^5 to 405, 365, and 254 nm light, respectively, outperforming other BCPs with 10^4 , 10^5 , and 10^2 for *PF-b-Piso*₁₀, *PF-b-Piso*₆₀, and *PF-b-Piso*₁₀₀, respectively. Next, Figure S10, Supporting Information, depicts the transfer characteristics of the *PF-b-Piso*₂₀-based device after 1–10 consecutive write/erase cycles, and the correlation of V_{th} in the ON/OFF states is summarized in Figure 4b. As can be seen, the memory device presented stable memory states with

high discrepancy, and the V_{th} level in the OFF state could be efficiently returned to that in the ON state after the photowriting process. The memory switching tests were manipulated with write–read–erase–read (WRER) cycle measurements with light programming as shown in Figure 4c,d and Figure S11, Supporting Information, for *PF-b-Piso*₂₀, and Figure S9d–f, Supporting Information, for *Piso*₁₀, *PF-b-Piso*₆₀, and *PF-b-Piso*₁₀₀, respectively. The photowriting or electrical erasing were conducted with 20 s light illumination at $V_d = -60$ V, or $V_g = -40$ V for 1 s at $V_d = -60$ V. In addition, UVA and UVC light were also applied in the WRER test on *PF-b-Piso*₂₀ based device. Although the electrical erasing gave rise to hole trapping in the BCP electret, the photoinduced exciton could split into electron/hole pair and the electron could repetitively recombine with the trapped hole in the BCP film, and the memory device could be written with light again. Therefore, *PF-b-Piso*₂₀ presents a highly stable I_{on}/I_{off} of 10^4 , 10^2 , and 10^3 to 405, 365, and 254 nm light, respectively, which is better than other BCPs with I_{on}/I_{off} of 10^2 , 10^3 , and 10^1 for *PF-b-Piso*₁₀, *PF-b-Piso*₆₀, and *PF-b-Piso*₁₀₀ with 405 nm light programming, respectively. Compared to our previous work with *PF-b-PS* as electret in the photonic FET memory, the current device with *PF-b-Piso* exhibited a higher I_{on}/I_{off} of 10^5 and 10^4 in the long-term retention test and memory endurance test compared to *PF-b-PS* with I_{on}/I_{off} of 10^4 and 10^3 , respectively.^[22] This improvement could be attributed to the stabilized electron trapped in the *PF-b-Piso* film with a larger ΔV_{th} . Therefore, the memory device with *PF-b-Piso* could be read without applying V_g to achieve a nondestructive readout and present higher memory stability.

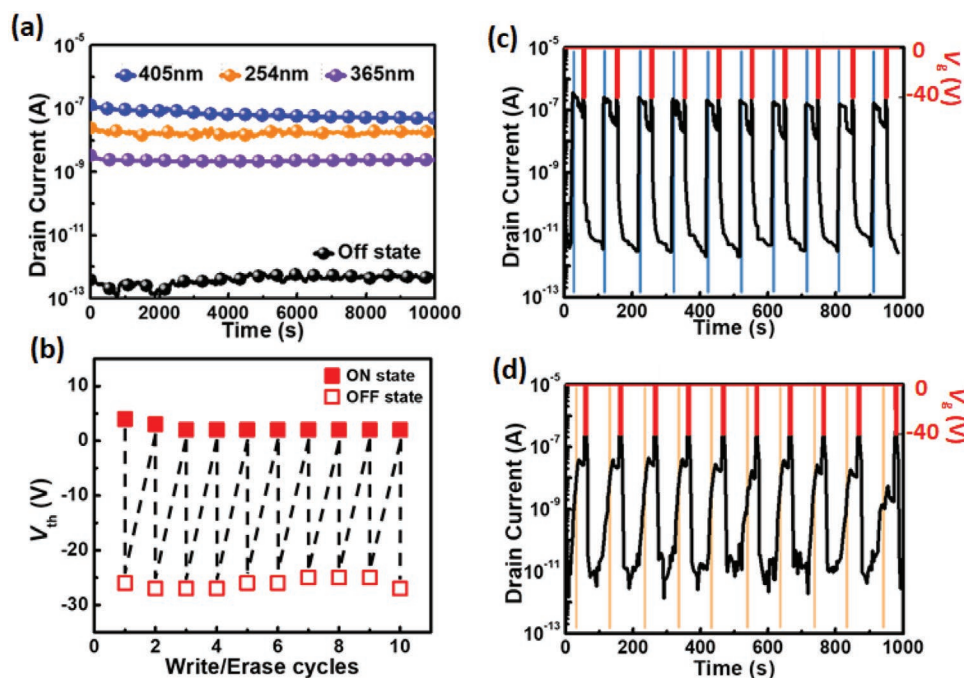


Figure 4. a) Long-term stability of the photonic FET memory device based on the annealed PF-*b*-Piso₂₀ film as the electret at $V_d = -60$ V and $V_g = 0$ V by photo-writing and electrical erasing. b) Correlation of the V_{th} in the ON/OFF states to the photowriting (405 nm; 30 mW cm⁻² for 20 s) / electrical erasing (-40 V; 1 s) cycles derived from the transfer characteristics. Memory endurance test of the photonic FET memory device based on the annealed PF-*b*-Piso₂₀ film as the electret with c) photo-writing (405 nm; 30 mW cm⁻² for 20 s) or d) photo-writing (254 nm; 0.9 mW cm⁻² for 20 s) and electrical erasing (-40 V; 1 s) cycle conducted at $V_d = -60$ V. Note that the top red line indicates the gate impetus applied for electrical erasing of the memory device, and the photo-writing and reading processes were measured at $V_d = -60$ V and $V_g = 0$ V.

To evaluate the transitions of photoresponse, different illumination time ranging from 1 to 80 s for PF-*b*-Piso₂₀ based device with blue, UVA, and UVC light were applied, as seen in Figure 5a and Figure S12a,b, Supporting Information, and the relevant characteristics of the devices with PF-*b*-Piso₁₀, PF-*b*-Piso₆₀, and PF-*b*-Piso₁₀₀ are presented in Figure S13a–c, Supporting Information, respectively. It can be seen that different stable levels of the ON-state current was obtained by giving light illumination for 1–20 s, and PF-*b*-Piso₂₀ could achieve a high I_{on}/I_{off} of 10⁴ and a medium I_{on}/I_{off} of 10² with 10 and 1 s of illumination with 405 nm light. In contrast, PF-*b*-Piso₁₀ and PF-*b*-Piso₁₀₀ presented a lower I_{on}/I_{off} of 10¹–10² with light illumination for 1–10 s. In addition, different programming V_d of -1 to -60 V were applied to the memory device during the photo writing process (Figure 5b, and a decent I_{on}/I_{off} of >10³ can be obtained with V_d of -5 V. Notably, green (530 nm) and red light (650 nm) according to the optical absorption band of pentacene, were applied to program the memory device with PF-*b*-Piso₂₀ electret (Figure 5c). Intriguingly, a decent I_{on}/I_{off} of 10⁴ and 10² were obtained with green and red light illumination, indicating that the photoinduced exciton can be transiently transduced into the BCP electret and form trapped charge to modulate the current level. This phenomenon is in coincidence with the previously reported system with poly(3-hexylthiophene) as channel layer and perovskite-based floating gate electret, which showed photoresponding to 650, 530, and 405 nm owing to the complementary optical absorption.^[31,32] The above results endow multilevel and multiband photoresponding of the memory device by applying suitable illumination time, and color of light with

650 and 530 nm (pentacene), 405 and 365 nm (PF), and 254 nm (Piso).

2.4. Operating Mechanism for Photo-Writing and Electrical Erasing of Photonic FET Memory Device

After characterizing the memory device performance, the operating mechanism of the photonic FET memory is next rationalized as shown in Figure 6. The BCP electrets were photowritten with blue, UVA, and UVC light as shown in Figure 6b,c, and this phenomenon could be attributed to the multiband absorption of PF and Piso. The photoinduced exciton was transiently transduced into hole and electron, and the former tunneled into the channel layer; while the latter was trapped between the interfaces of PF and Piso. The trapped charge was stabilized by favorable energy level adaptation. It is understood that the difference in the HOMO level between PF and pentacene could prevent carrier back-trapping; while a lower-lying LUMO level of insulating segment (Piso) is compared to PF, which is favorable for stabilizing trapped charges. As for applying a negative gate bias, a hole was possibly injected from the pentacene channel into the BCP electret to recombine the trapped electron (Figure 6d, and the memory device was recovered to its OFF state. Notably, the performance discrepancy between the BCP electrets can be attributed to two factors: 1) a higher amount of Piso coil is necessary to evenly distribute PF domain to stabilize the trapped charge; 2) PF plays an important role in transporting hole into channel layer for efficient exciton dissociation

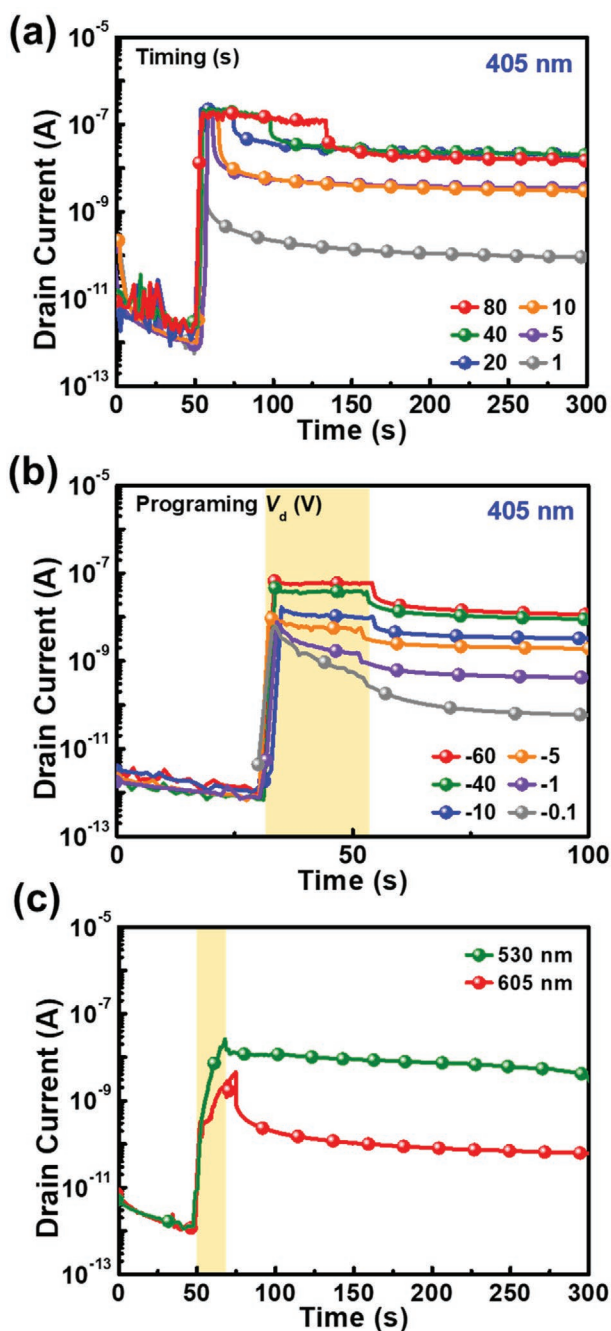


Figure 5. Transient characteristics of photonic FET memory based on the annealed PF-*b*-Piso₂₀ film as the electret with photo-writing of 405 nm; 30 mW cm⁻² for a) varied duration and programming V_d of -60 V; b) varied programming V_d and light illumination of 20 s; and c) different light sources of 530 nm; 10 mW cm⁻² or 650 nm; 5 mW cm⁻² for 20 s and programming V_d of -60 V. Note that all the drain current was measured at $V_g = 0$ V.

(Figure S14, Supporting Information). Therefore, an optimized BCP composition was obtained with PF-*b*-Piso₂₀ to render a conspicuous memory device performance with a high current contrast of 10^6 to 405 nm light and 10^5 to 254 nm light over 10^4 s. Ensuingly, the multilevel and multiband photoresponding of the memory device can be successfully achieved by applying suitable

illuminating time, and band of light with 650 and 530 nm (pentacene), 405 and 365 nm (PF), and 254 nm (Piso).

3. Conclusion

In conclusion, a series of PF based BCPs of PF-*b*-Piso was studied and applied as polymer electret in photonic FET memory. We found that the ratio between the conjugated and insulating segments in PF-*b*-Piso could pivotally affect the charge storage and photoresponse efficacy in the electret of photonic FET memory. Therefore, PF self-aggregation was successfully mitigated with an enhanced Piso content. Next, according to the UV-vis absorption bands of the BCPs with 350–410 nm for PF and 250–300 nm for Piso, a multiband photoresponding to blue, UVA, and UVC light was observed in the memory device. Consequently, an optimized composition was obtained with PF-*b*-Piso₂₀ to render a conspicuous memory device performance with a high current contrast of 10^6 to 405 nm light and 10^5 to 254 nm light over 10^4 s. In addition, current contrast of 10^4 and 10^2 was obtained with 650 and 530 nm light programming for the device with PF-*b*-Piso₂₀ as electret, and this phenomenon can be attributed to the charge transfer between channel and memory layers. The experimental results proved that BCP design conduces to form self-assembled microphase separation to stabilize the trapped charge in the polymer electret, and it warrants further investigation about the functionality of insulating coil with visible light absorption as BCP electret.

4. Experimental Section

Materials: Anhydrous chlorobenzene (CB, 99.8%) was purchased from Sigma Aldrich. Pentacene (sublimed, >99%) was purchased from Luminescence Technology Corp. PF-*b*-Piso was prepared based on the authors' previous work with chain-growth Suzuki–Miyaura coupling polymerization for poly[2,7-(9,9-dihexylfluorene)] (PF) and atom transfer radical polymerization (ATRP) for poly(pendent isoindigo) (Piso). The block copolymers (BCPs) studied were prepared by using a click reaction of copper-catalyzed azide–alkyne cycloadditions (CuAAC) with ethyne-terminated PF block ($M_{n,NMR} = 4900$) and azide-terminated Piso block with $M_{n,NMR} = 4900, 9900, 29\ 800,$ and $53\ 700$ for PF-*b*-Piso₁₀, PF-*b*-Piso₂₀, PF-*b*-Piso₆₀, and PF-*b*-Piso₁₀₀, respectively.

Characterization: UV-vis absorption spectrum was recorded by using a Hitachi U-4100 spectrophotometer. PL emission spectrum was recorded by using a Horiba Jobin Yvon Fluorolog-3 spectrofluorometer. Nanostructures of the BCP thin films were performed on AFM using a Nanoscope 3D controller AFM (Digital Instruments) under tapping mode. Commercial silicon cantilevers (Nanosensor PPP-SEIHR) were used with a spring constant of $15\ \text{N m}^{-1}$ and resonant frequency of 330 kHz, respectively. GISAXS and GIWAXS measurements of the polymer films on bare wafer substrates were collected on beamline BL23A1 in National Synchrotron Radiation Research Center (NSRRC), Taiwan. A monochromatic beam with a wavelength (λ) of $1.24\ \text{\AA}$ was used, and the incident angle was set as 0.16° . The scattering intensities are reported as intensity versus q , where $q = (4\pi/\lambda) \sin(\theta/2)$; λ is the wavelength of incident X-rays $1.240\ \text{\AA}$, and θ is the scattering angle.

Fabrication and Characterization of the Photonic FET Memory Devices: BCP solutions of PF-*b*-Piso_{*n*} ($n = 10, 20, 60, 100$) in CB ($5\ \text{mg mL}^{-1}$) were heated at $60\ ^\circ\text{C}$ for 8 h and passed through a PTFE membrane syringe filter with pore size of $0.22\ \mu\text{m}$. Then, the BCP solutions were spin-coated onto UV-pretreated silicon wafer with a 100-nm-thick SiO₂ layer at a spin

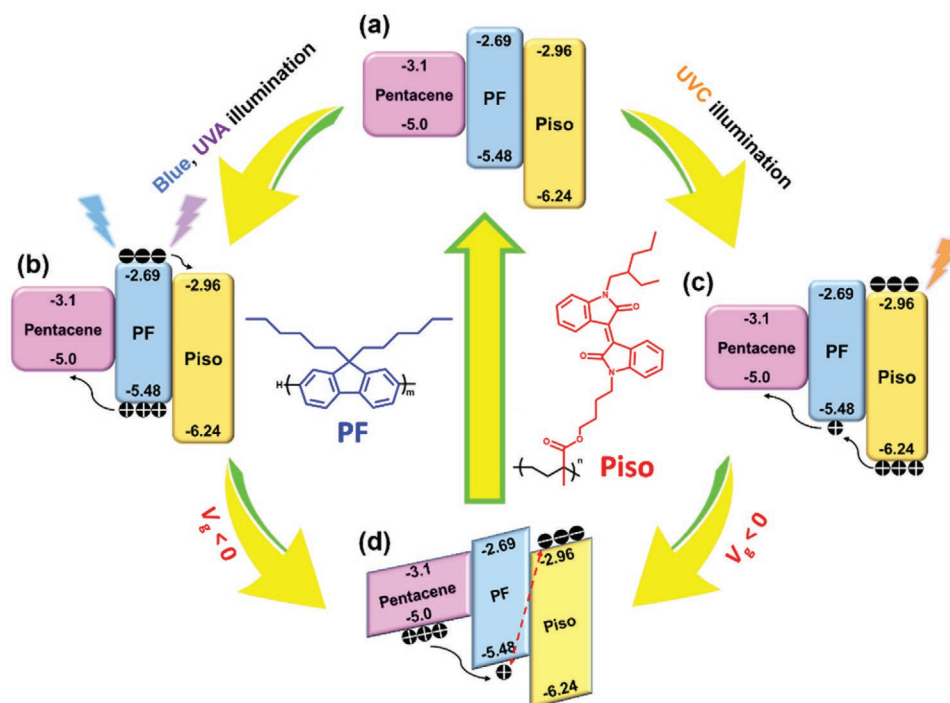


Figure 6. a) Energy level alignment of pentacene, PF, and Piso. b,c) Schematic illustration of the photo-writing process by using b) blue and UVA light or c) UVC light. d) Schematic illustration of the electrical erasing for recovering the photonic FET memory device to the OFF state of (a).

rate of 800–1000 rpm for 60 s. The BCP films were thermally annealed at 100 °C under a nitrogen atmosphere for 1 h. Then, a 50-nm-thick pentacene layer was thermally deposited onto the eletret layer at a rate of 0.2–0.3 nm/s at 9×10^{-7} Torr. Finally, 70-nm-thick gold were deposited through a regular shadow mask (channel width, $W = 1000 \mu\text{m}$; channel length, $L = 50 \mu\text{m}$) to define the source-to-drain channel electrodes.

The FET memory device characterization was conducted with a Keithley 4200-SCS semiconductor parameter analyzer with Remote PreAmp (4200-PA) in a N_2 -filled glovebox. The drain current (I_d) was measured at $V_d = -60$ V when applying photo-writing (405 nm; 30 mW cm^{-2} for 20 s, 254 nm; 0.916 mW cm^{-2} for 20 s, 365 nm; 0.916 mW cm^{-2} for 20 s) or electrical-erasing ($V_g = -40$ V; 1 s). The device was swept with V_g from 20 to -40 V and V_d of -40 V in the transfer characteristics. The field effect mobility (μ) and threshold voltage (V_{th}) were calculated from linear fitting in the saturation regime according to the following equation:

$$I_d = \mu \frac{W}{2L} C_{ox} (V_g - V_{th})^2 \quad (1)$$

where C_{ox} is the areal capacitance of a 100-nm-thick SiO_2 layer (31.5 nF cm^{-2}).

Supporting Information

Supporting Information is available from the Wiley Online Library or from the author.

Acknowledgements

The authors acknowledge the Featured Area Research Center Program within the framework of the Higher Education Sprout Project by the Ministry of Education (110L9006) and the Ministry of Science and Technology in Taiwan (MOST 110-2634-F-002-043) for financial support.

Conflict of Interest

The authors declare no conflict of interest.

Data Availability Statement

Research data are not shared.

Keywords

conjugated block copolymer, photomemory, photoprogramming, polyfluorene, polymer electret

Received: June 25, 2021
Revised: August 9, 2021
Published online: October 8, 2021

- [1] M. Chen, H. Nam, S. Wi, G. Priessnitz, I. M. Gunawan, X. Liang, *ACS Nano* **2014**, *8*, 4023.
- [2] Y. Zhai, J. Q. Yang, Y. Zhou, J. Y. Mao, Y. Ren, V. A. Roy, S. T. Han, *Mater. Horiz.* **2018**, *5*, 641.
- [3] Y. Yu, Q. H. Ma, H.-F. Ling, W. Li, R.-L. Ju, L. Y. Bian, N.-E. Shi, Y. Qian, M.-D. Yi, L.-H. Xie, W. Huang, *Adv. Funct. Mater.* **2019**, *29*, 1904602.
- [4] S. Dai, Y. Zhao, Y. Wang, J. Zhang, L. Fang, S. Jin, Y. Shao, J. Huang, *Adv. Funct. Mater.* **2019**, *29*, 1903700.
- [5] P. Heremans, G. H. Gelinck, R. Muller, K.-J. Baeg, D.-Y. Kim, Y.-Y. Noh, *Chem. Mater.* **2011**, *23*, 341.
- [6] C. Liu, H. Chen, X. Hou, H. Zhang, J. Han, Y. G. Jiang, X. Zeng, D. W. Zhang, P. Zhou, *Nat. Nanotechnol.* **2019**, *14*, 662.

- [7] Z. Zhu, Y. Guo, Y. Liu, *Mater. Chem. Front.* **2020**, *4*, 2845.
- [8] C. C. Shih, W. Y. Lee, W. C. Chen, *Mater. Horiz.* **2016**, *3*, 294.
- [9] F. Sun, Q. Lu, L. Liu, L. Li, Y. Wang, M. Hao, Z. Cao, Z. Wang, S. Wang, T. Li, *Adv. Mater. Technol.* **2020**, *5*, 1900888.
- [10] D. Hao, J. Zhang, S. Dai, J. Zhang, J. Huang, *ACS Appl. Mater. Interfaces* **2020**, *12*, 39487.
- [11] W. C. Yang, Y. C. Lin, M. Y. Liao, L. C. Hsu, J. Y. Lam, T. H. Chuang, G. S. Li, Y. F. Yang, C. C. Chueh, W. C. Chen, *ACS Appl. Mater. Interfaces* **2021**, *13*, 20417.
- [12] H. Wei, Y. Ni, L. Sun, H. Yu, J. Gong, Y. Du, M. Ma, H. Han, W. Xu, *Nano Energy* **2021**, *81*, 105648.
- [13] J. Y. Chen, Y. C. Chiu, Y. T. Li, C. C. Chueh, W. C. Chen, *Adv. Mater.* **2017**, *29*, 1702217.
- [14] E. Ercan, Y.-C. Lin, L.-C. Hsu, C.-K. Chen, W.-C. Chen, *Adv. Mater. Technol.* **2021**, *6*, 2100080.
- [15] C. C. Shih, Y. C. Chiang, H. C. Hsieh, Y. C. Lin, W. C. Chen, *ACS Appl. Mater. Interfaces* **2019**, *11*, 42429.
- [16] Y. Park, K. J. Baeg, C. Kim, *ACS Appl. Mater. Interfaces* **2019**, *11*, 8327.
- [17] Y.-C. Chiang, C.-C. Hung, Y.-C. Lin, Y.-C. Chiu, T. Isono, T. Satoh, W. C. Chen, *Adv. Mater.* **2020**, *32*, 2002638.
- [18] C.-C. Hung, Y.-C. Chiang, Y.-C. Lin, Y.-C. Chiu, W.-C. Chen, *Adv. Sci.* **2021**, *8*, 2100742.
- [19] C. H. Chen, Y. Wang, H. Tatsumi, T. Michinobu, S. W. Chang, Y. C. Chiu, G. S. Liou, *Adv. Funct. Mater.* **2019**, *29*, 1902991.
- [20] C. H. Chen, Y. Wang, T. Michinobu, S. W. Chang, Y. C. Chiu, G. S. Liou, *ACS Appl. Mater. Interfaces* **2020**, *12*, 6144.
- [21] C.-Y. Ke, M.-N. Chen, M.-H. Chen, Y.-T. Li, Y.-C. Chiu, G.-S. Liou, *Adv. Funct. Mater.* **2021**, *31*, 2101288.
- [22] Y. C. Chen, Y. C. Lin, H. C. Hsieh, L. C. Hsu, W. C. Yang, T. Isono, T. Satoh, W. C. Chen, *J. Mater. Chem. C* **2021**, *9*, 1259.
- [23] Y.-F. Yang, Y.-C. Chiang, Y.-C. Lin, G.-S. Li, C.-C. Hung, W.-C. Chen, *Adv. Funct. Mater.* **2021**, 2102174.
- [24] U. Scherf, E. J. List, *Adv. Mater.* **2002**, *14*, 477.
- [25] L. H. Xie, C. R. Yin, W. Y. Lai, Q. L. Fan, W. Huang, *Prog. Polym. Sci.* **2012**, *37*, 1192.
- [26] A.-N. Au-Duong, C. C. Wu, Y. T. Li, Y. S. Huang, H. Y. Cai, I. J. Hai, Y. H. Cheng, C. C. Hu, J. Y. Lai, C. C. Kuo, Y. C. Chiu, *Macromolecules* **2020**, *53*, 4030.
- [27] C. C. Shih, Y. C. Chiu, W. Y. Lee, J. Y. Chen, W. C. Chen, *Adv. Funct. Mater.* **2015**, *25*, 1511.
- [28] M. Kang, D. Khim, J. Kim, H. J. Lee, J. Y. Jo, K. J. Baeg, D. Y. Kim, *Org. Electron.* **2018**, *58*, 12.
- [29] L. C. Hsu, T. Isono, Y. C. Lin, S. Kobayashi, Y. C. Chiang, D. H. Jjiang, C. C. Hung, E. Ercan, W. C. Yang, H. C. Hsieh, *ACS Appl. Mater. Interfaces* **2021**, *13*, 2932.
- [30] J. T. Wang, K. Saito, H. C. Wu, H. S. Sun, C. C. Hung, Y. Chen, T. Isono, T. Kakuchi, T. Satoh, W. C. Chen, *NPG Asia Mater* **2016**, *8*, e298.
- [31] Y. H. Chang, C. W. Ku, Y. H. Zhang, H. C. Wang, J. Y. Chen, *Adv. Funct. Mater.* **2020**, *30*, 2000764.
- [32] H. Hsu, D. Yang, L. D. Wiyanto, J. Chen, *Adv. Photonics Res.* **2021**, *2*, 2000185.